17th Brazilian Congress of Thermal Sciences and Engineering
November 25th-28th, 2018, Águas de Lindóia, SP, Brazil

ENCIT-2018- 0759
PRESSURE AND SHEAR STRESS ANALYSIS IN A TRIANGULAR TUBE BUNDLE BASED ON EXPERIMENTAL FLOW VELOCITY FIELD

Douglas Martins Rocha
Department of Mechanical Engineering, São Carlos School of Engineering, University of São Paulo, São Carlos, SP, Brazil
douglas.rocha@usp.br

Fabio Toshio Kanizawa
Department of Mechanical Engineering, School of Engenerring, Universidade Federal Fluminense, Niterói, RJ, Brazil
fabiokanizawa@id.uff.br

Kosuke Hayashi
Graduate School of Engineering, Kobe University, 1-1, Rokkodai, Nada, Kobe 657-8501, Japan.
hayshi@kobe-u.ac.jp

Shigeo Hosokawa
Graduate School of Engineering, Kobe University, 1-1, Rokkodai, Nada, Kobe 657-8501, Japan.
hosokawa@kobe-u.ac.jp

Akio Tomiyama
Graduate School of Engineering, Kobe University, 1-1, Rokkodai, Nada, Kobe 657-8501, Japan.
tomiyama@mech.kobe-u.ac.jp

Gherhardt Ribatski
Department of Mechanical Engineering, University of São Paulo, São Carlos School of Engineering, São Carlos, SP, Brazil
ribatski@sc.usp.br

Abstract. *This paper presents the experimental vector velocity field obtained in a triangular tube bundle with tubes of 20 mm O.D. and transverse pitch of 25.2 mm based on the Spatial Filter Velocimetry technique. The experiments were conducted under single-phase water flows with Reynolds ranging from 443 to 1842. Based on the experimental results, the pressure was estimated by solving the Poisson equation, and the shear stress around the tubes was estimated calculating the viscous and Reynolds stresses. The turbulence strength and the flow vorticity were calculated and discussed to analyze the flow structure. All the analyses were performed using a second order finite difference scheme to estimate the partial derivatives. The results indicate that the Spatial Filter Velocimetry technique provides accurate velocity data and is suitable to be applied in complex geometries.*

Keywords: *External flow, Tube-bundle, Spatial Filter Velocimetry, Velocity field.*

1. NOMENCLATURE

Roman symbols

$\bar{P}$ average pressure [Pa]
x relative to x axis [m]
y relative to y axis [m]
z relative to z axes [m]
U actual velocity [m]
$\bar{U}$ average velocity [m/s]
u velocity fluctuation [m/s]
u^{rms} turbulence strength [m/s]
I image intensity [-]
F filter [-]
t time [s]
f frequency [Hz]
L spacing between each strip of the spatial filter [μm]
d distance [m]
Q volumetric flow rate [l/min]
j superficial velocity [m/s]
v resultant velocity [m/s]
Re Reynolds number

Greek symbols

ρ phase density [kg/m³]
τ shear stress [Pa]
μ viscosity [Pa.s]
ω vorticity [1/s]

Subscripts
i index notation
j index notation
l relative to liquid phase
SF spatial filter applied
D dominant frequency

2. INTRODUCTION

Shell and tube heat exchangers are widely used in simple and complex systems such as air conditioning systems, chillers, and steam generators. This fact highlights the importance of studies focused on external flows and heat transfer across tube bundles heat exchangers. However, as pointed out by Kanizawa and Ribatski (2016a,b) the number of publication focused on external flows across tube bundles is considerably lower than those focused on internal flows because of the geometric complexity of these devices. Paul *et al.* (2007) indicate that the majority of the studies performed for external flows across tube bundles are focused on global results such as the void fractions and the total pressure drop. Although these studies provide useful information to improve understanding of the flow phenomenology, they are generally restricted to a specific experimental apparatus and do not provide information about local parameters. Therefore, in order to completely understand different flow parameters, such as heat transfer coefficient, pressure drop and flow-induced vibrations, detailed experimental results about the local flow structure are required. In this context, the flow velocity measurements based on optical techniques, which are generally nonintrusive methods, are attracting the interest of academic community and industry because of their accuracy and the capability of providing detailed results.

According to Hosokawa and Tomiyama (2012), the optical flow velocimetry techniques can be categorized as a time of flight (ToF) or distance of flight (DoF) based techniques, and most of them require tracer particles dispersed in the fluid. In the ToF techniques, the particle velocity is determined by the period of displacement of the particle in a region of known size. On the other hand, in the DoF techniques, the particle velocity is determined by the displacement of the particle during a known period. The Particle Image Velocimetry (PIV) and the Laser Doppler Velocimetry (LDV) are examples of DoF and ToF techniques, respectively. The relative errors of the ToF techniques are directly proportional to the velocity and they can be reduced by increasing the sampling frequency, making them very accurate. On the other hand, although for low velocities the accuracy of the DoF is lower than of the ToF techniques, the DoF is more versatile, as the PIV technique, and they allow to evaluate the velocity of several particles at the same time, which is usually impossible for ToF methods. Recently, Hosokawa and Tomiyama (2012) developed a Spatial Filter Velocimetry (SFV) technique based on time-series particle images that combines the accuracy of the ToF techniques and the benefit of measuring several particle images at the same time.

Iwaki *et al.* (2005) highlighted that the use of laser velocimetry techniques in heat exchanger analyses is very promising, but the number of experimental investigations based on the velocity field measurement during cross-flow in tube bundles is limited. In this context, Iwaki *et al.* (2004) and Paul *et al.* (2007) detailed the flow field for single-phase cross-flow in staggered and in line tube bundles by using PIV, obtaining results for vector velocity field, vortex structure and turbulence intensity. Paul *et al.* (2007) concluded that downstream the first row of tubes there is large and intense vortices that diminish considerably along the flow path. A similar result was obtained by Iwaki *et al.* (2004), who conclude that such behavior justifies the short distance for the full development of the flow in staggered arrays compared with in-line arrays. In the same token, Iwaki *et al.* (2005) analyzed the two-phase flow structure across tube bundles using PIV, however, the authors used a shallow test section which might affect the velocity profile.

Hosokawa *et al.* (2013) discussed the difficulties to perform optical measurements during multiphase flows in complex geometries, and developed a submersible small fiber LDV probe to measure velocity distribution in a tube bundle test section. Using the SFV technique, Hosokawa and Tomiyama (2012) obtained the velocity field of laminar and turbulent flows in a rectangular test section with accuracy as high as in LDV technique. The results obtained by Hosokawa and Tomiyama (2012) indicate that the SFV technique is a suitable tool to be applied in studies of the flow field in tube bundles test sections.

Based on the above discussed, the present study presents an experimental investigation of the vector velocity field, and the pressure and shear stress distribution during single-phase flow across tube bundle using the SFV technique proposed by Hosokawa and Tomiyama (2012). The velocity field was obtained in a triangular tube bundle test section with tubes of 20 mm O.D., transverse pitch of 25.2 mm and Reynolds ranging from 443 to 1842, with experiments performed by Kanizawa (2016) at Kobe University.

3. EXPERIMENTAL INVESTIGATION

The experimental apparatus located at Kobe University and illustrated in Fig. 1 was basically composed by a tube bundle test section (Fig. 1a) made of acrylic to analyze the single-phase water flow. The water was propelled by a centrifugal pump (0.75 kW) from the lower reservoir; then it was directed to the volumetric flow rate measurement section composed by two rotameters with measuring ranges from 0.06 to 0.60 m³/h and from 0.2 to 2.0 m³/h and nominal uncertainties of ±5% F.S; then the water was injected in the bottom of the test section. The normal triangular

tube bundle test section was composed of 10 rows of 3 tubes, each with 20 mm O.D. mounted with a transversal pitch of 25.2 mm, corresponding to a pitch to diameter ratio of 1.26. An upper reservoir downstream of the test section was used to avoid pressure fluctuations in the test section, and then the liquid was directed to the lower reservoir. The complete details of the experimental apparatus can be found in Kanizawa (2016). The tubes are 100 mm long, and the measuring plane is 25 mm distant from the test section internal surface.

An optical system was developed for the laser sheet generation and camera installation schematically depicted in Fig. 1b. The laser source was installed in the opposite side of the high-speed video camera and was axially aligned with one of the hollow tubes. A support with a mirror inclined 45° in relation to the tube axis was inserted in the tube. Thus, the vertical laser sheet from the laser source was reflected to be perpendicular to the tube axis and to the camera line of sight. An optical rotary mount could rotate the mirror support and the laser source to better adjust the laser sheet position. The images were acquired at 12,500 fps using a high-speed video camera Photron FASTCAM SA-X2, equipped with a macro lens Micro Nikkor 60 mm f/2.8D.

The images were captured in the smallest possible areas to obtain the maximum spatial resolution, which contained the fundamental flow field of the test section. Based on the geometry of the tube bundle test section depicted in Fig. 1, and considering fully developed flow, it is possible to assume that the flow fields in similar geometry, such as depicted in Fig. 2, is invariable from row to row. Therefore, as schematically depicted in Fig. 2, two fundamental regions are identified in a normal triangle tube bundle, the upper (*Ur*) and lower (*Lr*) fundamental regions, for which the flow characteristics repeat along the tube bundle.

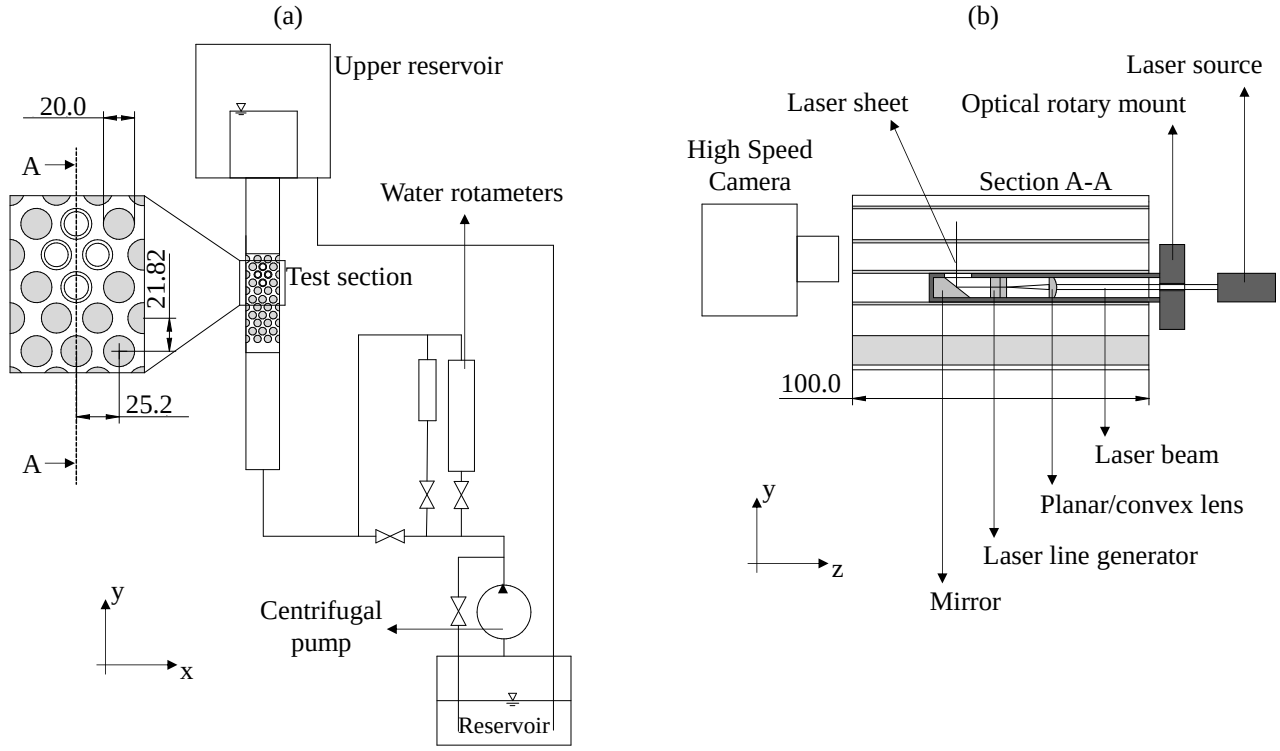

Figure 1. Experimental apparatus composed by a tube bundle test section made of acrylic (a) and an optical system (b) (dimensions in millimeter).

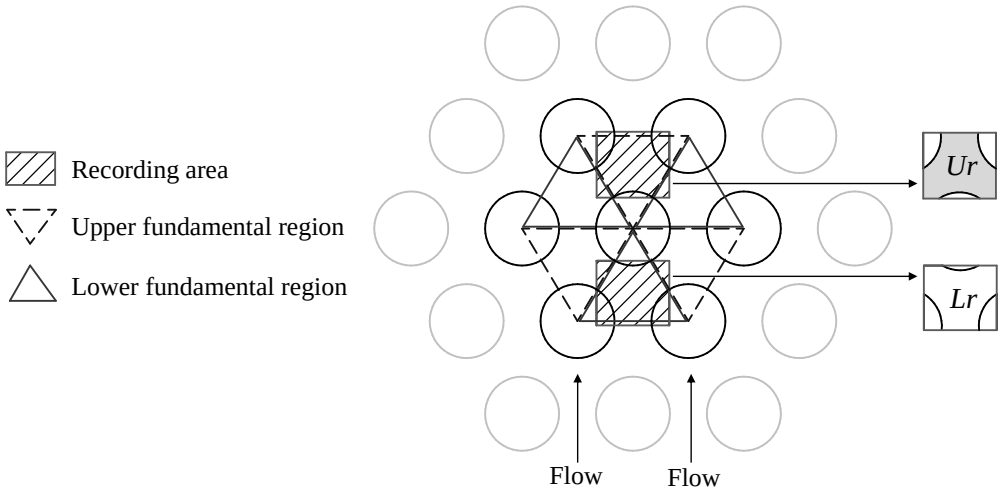

Figure 2: Regions of measurements based on the fundamental regions of the flow field.

4. METHOD OF ANALYSIS

In this paper, the vector velocity field was obtained by the SFV technique with the procedure schematically depicted in Fig. 3. Hosokawa and Tomiyama (2012) described the spatial filter velocimetry method based on a frequency analysis of time-series particle images, where the spatial filter was applied in a post-processing step via software. This new approach proposed by Hosokawa and Tomiyama (2012) makes the traditional SFV technique more flexible, allowing the change of fixed parameters related to the spatial filter, such as the spatial frequency, the type of spatial filter and the frequency shifting. According to Hosokawa and Tomiyama (2012), their method can be considered as a software LDV, because it simulates by image processing the fringe lines generated by the laser beam superposition in the LDV.

As can be seen in Fig. 3, images of the flow containing tracer particles with high definition must be acquired at high frame rate to obtain the vector velocity field, to ensure high spatial and temporal resolution. The particle illumination can be performed by any light source, as long as it provides enough brightness. Laser sheets provide good experimental results because their small thickness ensures low out of plane motion. Since the particles are theoretically moving at the same flow velocity, it is possible to infer the flow velocity from the particles velocities. In this paper, silicon carbide particles with an average size of 3 μm were used as tracer particles.

During the post-processing step, the area of interest is discretized into small interrogation areas, where spatial filters are applied in x (F_{SFx}) and y (F_{SFy}) directions. The spatial filters are applied on the image intensity (I) in each interrogation area to obtain the integral of the image intensity in the time domain ($I_{SFx}(t)$ and $I_{SFx}(t)$). The terms I_{SFx} and I_{SFy} illustrated in Fig.1 possess a periodic signal, in which the dominant frequencies (f_{Dx} and f_{Dy}) are obtained with a wavelet transform. These frequencies are directly proportional to the particle velocities v_x and v_y and inversely proportional to the filters wavelengths L_x and L_y, respectively, as illustrated in Fig. 3.

Thus, performing a frequency analysis of the filtered signal it is possible to evaluate the x and y components of the velocity for the given interrogation area. The same process is performed for all interrogation areas; therefore, the x and y components of the velocity are evaluated for the entire area of interest. The spatial resolution of the vector velocity field obtained is given by the size of the interrogation areas. In this work, the analysis steps described before of the Spatial Filter Velocimetry was performed by a code developed by the research group of Professor Akio Tomiyama at Kobe University in C++ language with the use of OpenCV libraries. Later, considering the discrete results obtained by the SFV technique, the experimental vector velocity field was analyzed to obtain the turbulence strength, the flow vorticity and the pressure and shear stress distribution around the tubes.

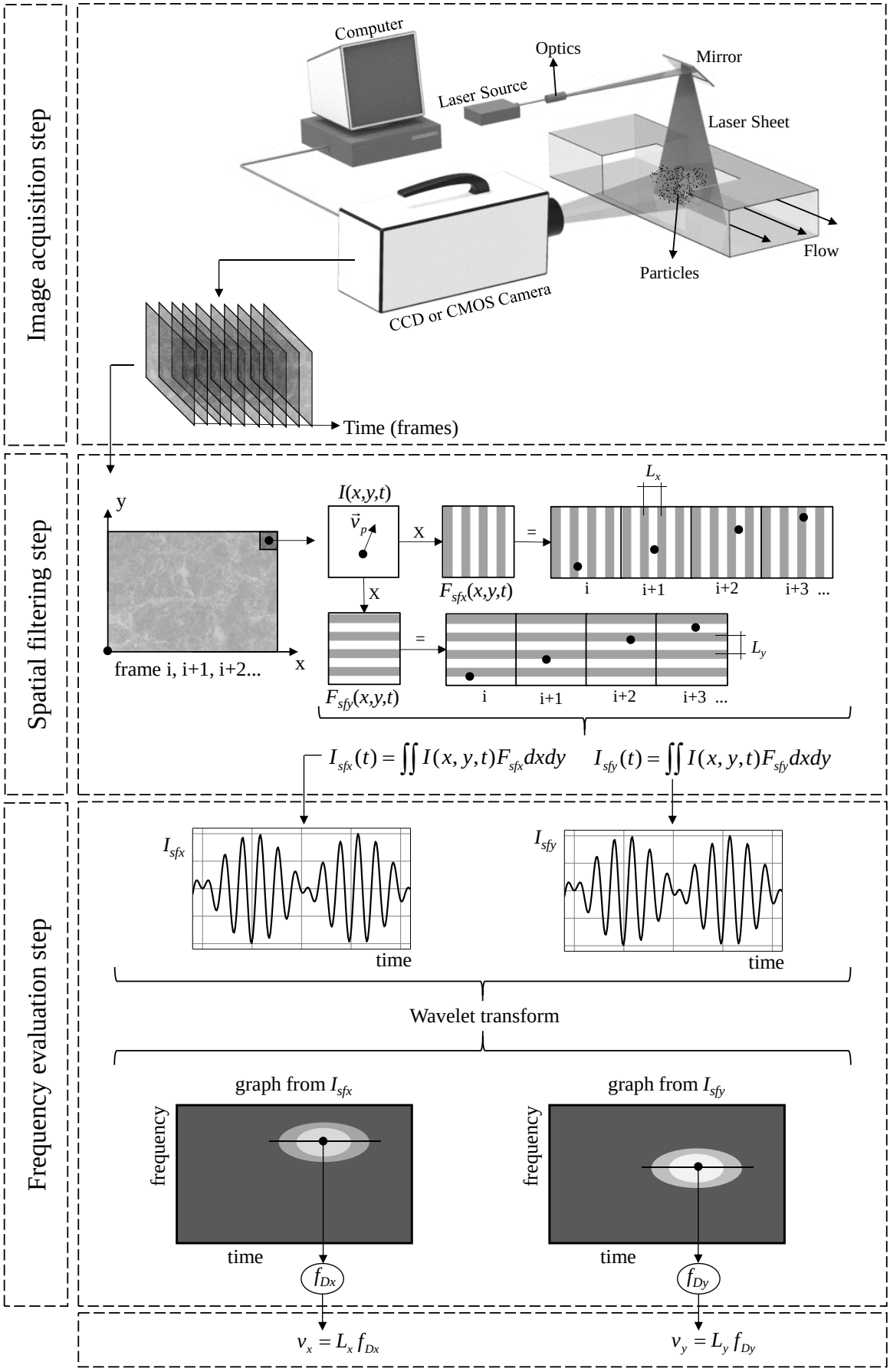

Figure 3. Schematics of the execution steps of the SFV technique (Adapted from Hosokawa and Tomiyama, 2012).

5. RESULTS AND DISCUSSION

This section presents the experimental results for velocity, shear stress and pressure fields during water single-phase flow across staggered tube bundle.

5.1 Vector velocity field and vorticity

Fig. 4 illustrates the vector velocity field obtained for each experimental condition in the regions *Ur* and *Lr* depicted in Fig. 2. The vector velocities presented in Fig. 4 are mean values of the time series results obtained from the SFV technique application. The images were acquired with an acquisition rate of 12,500 fps resulting in 87000 frames or 7 seconds of analysis. The spatial resolution of the images acquired by the high-speed camera was 15 μm/pixel. The areas of analysis showed in Fig. 4 comprise a rectangular shape of approximately 15 mm X 16 mm subdivided into 900 interrogation areas, which results in an average spatial resolution of measurement of 0.5 mm/interrogation area.

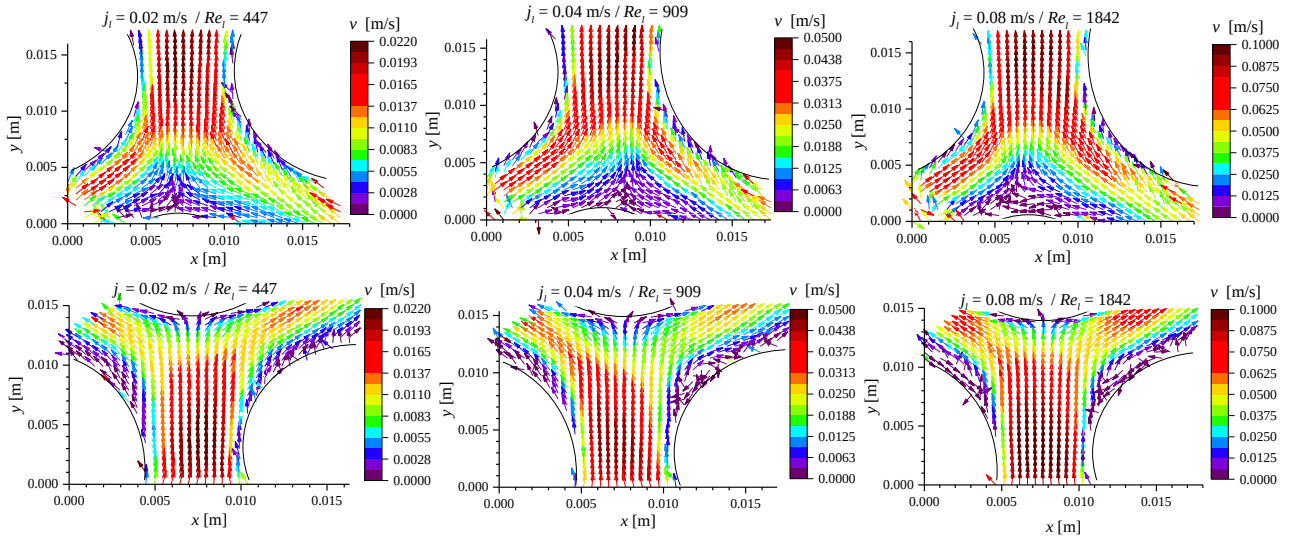

Figure 4: Flow velocity field obtained by the SFV technique application in the regions *Ur* (upper graphs) and *Lr* (lower graphs) defined in Fig 2.

As can be seen in Fig. 4 the highest velocities occurred in the center between two adjacent tubes, with velocity profile approximately parabolic, and the lowest velocities occurred near the tube wall because of the no-slip condition, both aspects in agreement with expected. Moreover, it is possible to identify recirculating zones just downstream the horizontal tubes centerline, more pronounced for highest Reynold numbers, which occurred due to the boundary layer detachment.

Additionally, according to Fig. 4 the velocity field symmetry increases with superficial flow velocity. This phenomenon was observed by Kanizawa (2016) and, according to De Paula *et al.* (2012), this result is related to the bistable behavior of the flow for reduced Reynolds numbers. In these conditions, the flow presents preferable paths of higher velocity, and from time to time, the path is switched to another configuration. Thus, even considering that mean values are presented in Fig. 4, the result still shows asymmetric velocity profile due to the longer period in one of the conditions.

The flow rate was estimated based on the velocity profile to check the validity of the adopted velocimetry method, by assuming developed and two-dimensional flow (negligible variation along tubes axis), and Fig. 5 presents the volumetric water flow rates obtained with the integration in *x*-direction of the *y* velocity component in several cross sections. This figure also depicts the flowrate measured with the rotameter, and according to this figure it can be concluded that both results are in good agreement, and that the SFV technique can be considered validated. The curves of the calculated volumetric flow rates strongly differ from the measured volumetric flow rates for conditions that it is impossible to integrate the *y* velocity component between two consecutive tubes in *x*-direction.

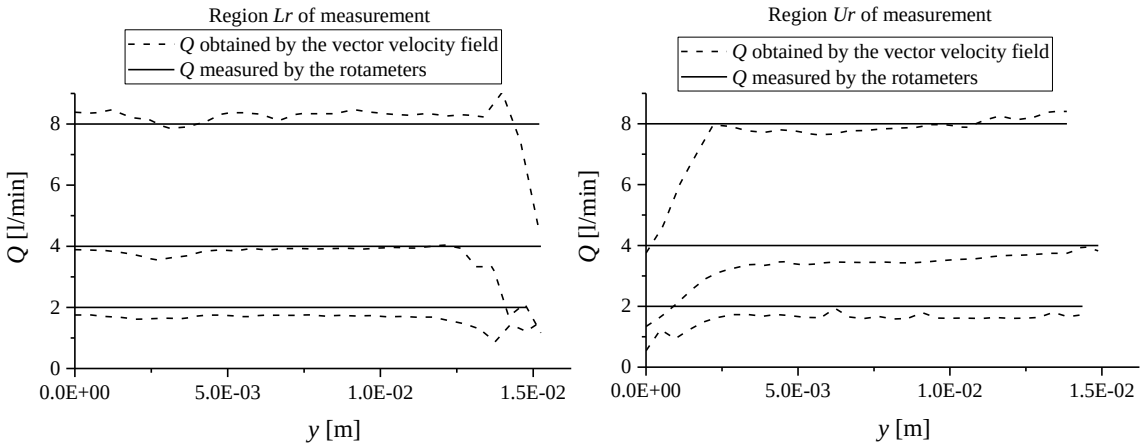

Figure 5: Comparison between the volumetric flow rates obtained by the water rotameters and estimated by the integration of the vector velocity field illustrated in Fig. 4.

Fig. 6 shows the flow vorticity estimated for the velocity fields presented in Fig. 4, which was calculated in the *xy* plane (see Fig(1)) according to the following equation:

$$\omega_z = \frac{\partial \bar{U}_y}{\partial x} - \frac{\partial \bar{U}_x}{\partial y} \tag{1}$$

where $\bar{U}$ refers to the mean velocity and subscripts *x*, *y* and *z* corresponds to the coordinates.

The partial derivatives of the Eq. (1) were calculated by a second-order finite difference scheme.

As depicted in Fig. 6, the positive and negative values of the flow vorticity occur in opposite sides of the flow passage, following the tube curvature in a similar way to the results obtained by Iwaki et al. (2004). The positive values of vorticity occur in the region where the flow has a clockwise rotation, whereas the negative values occur for an anticlockwise rotation. In the vertical tubes centerline, the flow vorticity reaches to zero because of the boundary layer intersection of each tube. The highest and lowest vorticity values are close to the tube wall, especially in the horizontal tube centerlines, where the velocity gradient has the highest values.

According to the Fig. 6, the lower regions (region *Lr* in Fig. 2) has the highest absolute values of vorticity and the regions where those values occur are thicker when compared to the upper regions (region *Ur* in Fig.2). This effect occurs because of the flow separation, which increases the flow vorticity values and is suppressed in the upper regions and induced in the lower regions.

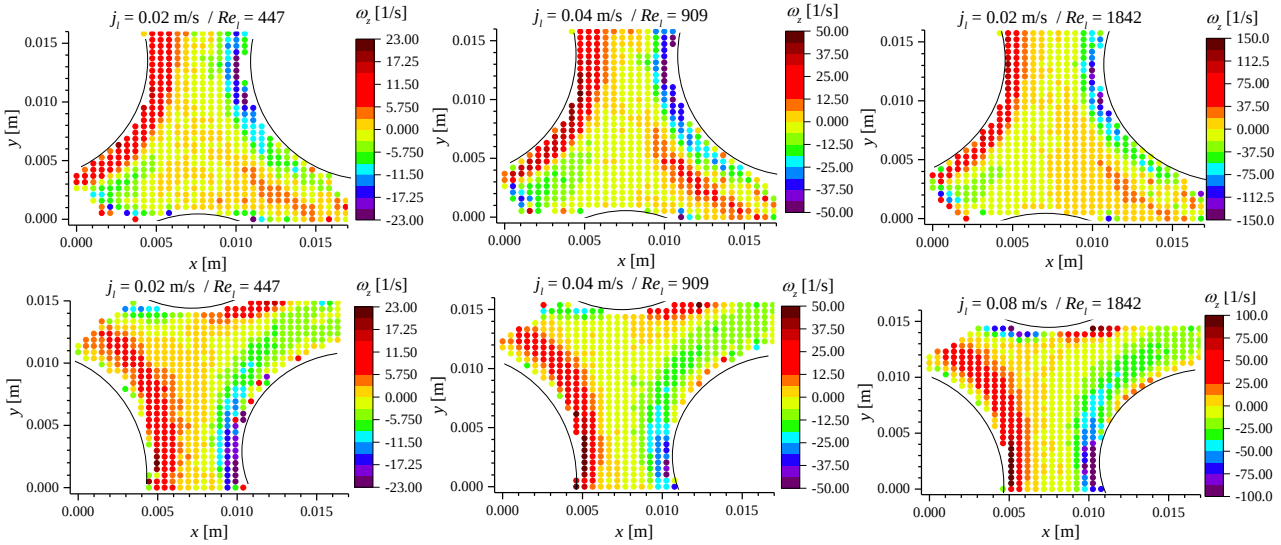

Figure 6: Flow vorticity of the regions *Ur* (upper graphs) and *Lr* (lower graphs) obtained from the vector velocity fields presented in Fig. 4.

5.2 Turbulence strength

Although the vector velocity field provides much information about the flow structure, it is important to analyze parameters directly related to the velocities fluctuations. The turbulence strength, for example, provides information about the turbulence distribution in the flow field, which allows identifying regions of high and low. In this study, the turbulence strengths are calculated with the root mean square (RMS) value of the velocities fluctuations as follow:

$$u^{rms}_{mn} = \sqrt{\frac{1}{N}\sum_{k=1}^{N}\left[\frac{(u_i)^2 + (u_j)^2}{2}\right]_k} \tag{2}$$

where u refers to velocity fluctuation, and subscripts m and n correspond to coordinates x and/or y. The term N corresponds to the number of datapoints.

Fig. 7 depicts the turbulence strength along the evaluated regions, and according to this figure the highest values of u^{rms}_{xx} occur in the regions of maximum velocities in x-direction and in the streamlines meeting. The highest values of u^{rms}_{yy} occur near to the recirculating zone and in the region of maximum velocities in y-direction. The highest values of u^{rms}_{xx} and u^{rms}_{yy} present the same magnitudes indicating a high flow mixing (Iwaki *et al.*, 2004). The slightly lower values of u^{rms}_{xy} compared with u^{rms}_{xx} and u^{rms}_{yy} indicate that the peak values of u_{xx} and u^{rms}_{yy} do not occur necessarily at the same time.

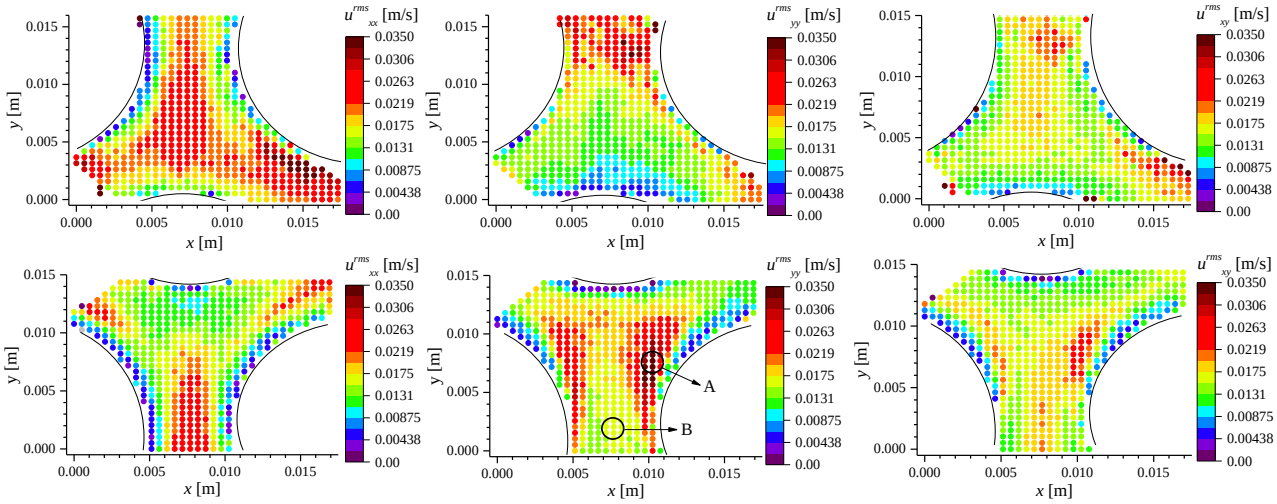

Figure 7: Turbulence strengths in x-direction (u^{rms}_{xx}), in y-direction (u^{rms}_{yy}) and of the resultant velocity (u^{rms}_{xy}) for the Reynolds number of 1842. The letter A indicates the region of maximum values of u^{rms}_{yy} and the letter B the region of maximum velocity, according to the Fig. 4.

Fig. 8 shows the differences between the behavior of the flow velocities in the recirculating zone (region A in Fig.7) and in the region of maximum velocity (region B in Fig. 7), by depicting the y velocity component along time and the corresponding histogram. As depicted in Fig. 7, the recirculating region has the highest values of u^{rms}_{yy}, even though the velocities of this region are intermediate (Figure 4, Re = 1842). As illustrated in Fig. 8, the velocity variation in the recirculation region is higher than that in the maximum velocity region, which justify the highest turbulence strength in the lower velocity region. The histogram of the flow velocity in region B is sharp and narrow, which indicates non-occurrence of peak-locking (Hosokawa and Tomiyama, 2012) and a well-defined flow direction. On the other hand, the flow velocity histogram in region A is soft and wide, mainly because of the recirculating zone, which causes a great variation of the flow velocity.

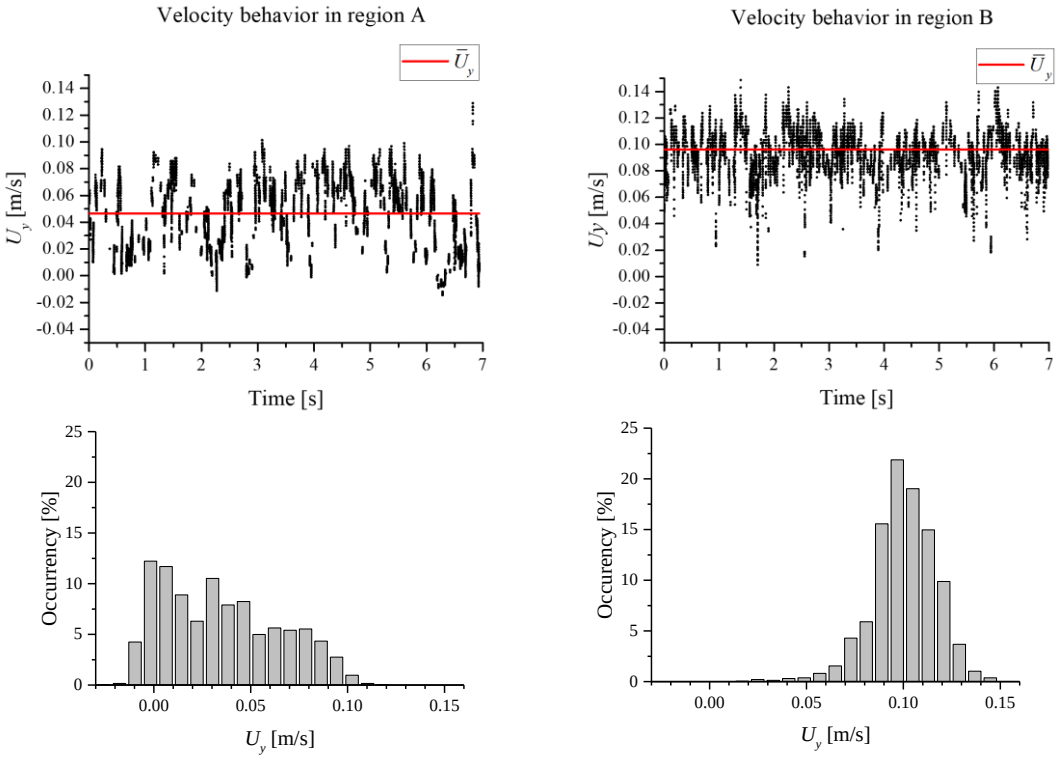

Figure 8: Velocity behavior along the acquisition time (upper graphs) and velocities histograms (lower graphs) in the regions A and B depicted in Fig. 7

5.3 Shear stress and pressure distribution

The shear stress around the tubes is related to a parcel of the drag and lift forces across the tube bundle. The viscous shear stress is dominant close to a solid wall, and the Reynolds turbulent stresses dominate the total shear stress in an outer region. Therefore, the analyses of the shear stress in the entire boundary layer provide also information about the flow structure. The total shear stress tensor can be written according to the following equation:

$$\tau_{ij} = \underbrace{\mu\left(\frac{\partial \bar{U}_i}{\partial x_j} + \frac{\partial \bar{U}_j}{\partial x_i}\right)}_{\tau^v} - \underbrace{\rho\overline{u_i u_j}}_{\tau^t} \tag{3}$$

where the first term of the RHS corresponds to the viscous shear stress tensor and the second term corresponds to the Reynolds turbulent stress tensor. The flow structure of the external flow obtained in the test section described in section 3 was analyzed in a two-dimensional domain (in a plane perpendicular to tube axes) because the effects of the velocity variation in z-direction (see Fig (1)) are negligible compared with the other directions, as demonstrated previously.

Fig. 9 and 10 show the viscous, turbulent and total shear stresses for Reynolds numbers of 447 and 1842, respectively. As depicted in Fig 9 and 10, the maximum absolute values of the viscous shear stresses occur close to the tube wall in the cross section passing by tubes centerline, because of the high-velocity gradient. Conversely, and as expected, the maximum Reynolds turbulent stress values occur away from the walls in regions of high velocities. The highest total shear stress observed for the Reynolds number of 447 is considerably lower (approximately 15 times) than that for the Reynolds number of 1842.

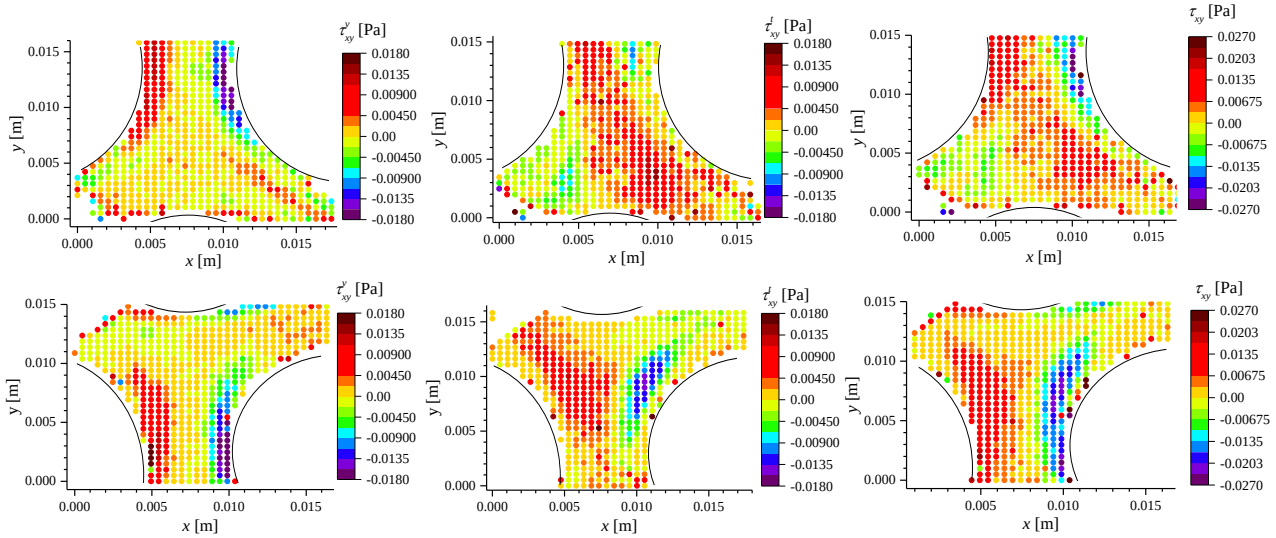

Figure 9: Viscous (τ_{xy}^{v}), Reynolds (τ_{xy}^{t}) and total (τ_{xy}) shear stresses for the Reynolds number of 447.

For *Re* of 447, presented in Fig. 9, the viscous and turbulent shear stresses have equivalent magnitudes. However, for *Re* = 1842, presented in Fig. 10, the maximum absolute value of the turbulent shear stress is approximately twice than the maximum value of the viscous shear stress. Therefore, the turbulent shear stress for the Reynolds number of 1842 represents a significant parcel of the total shear stress.

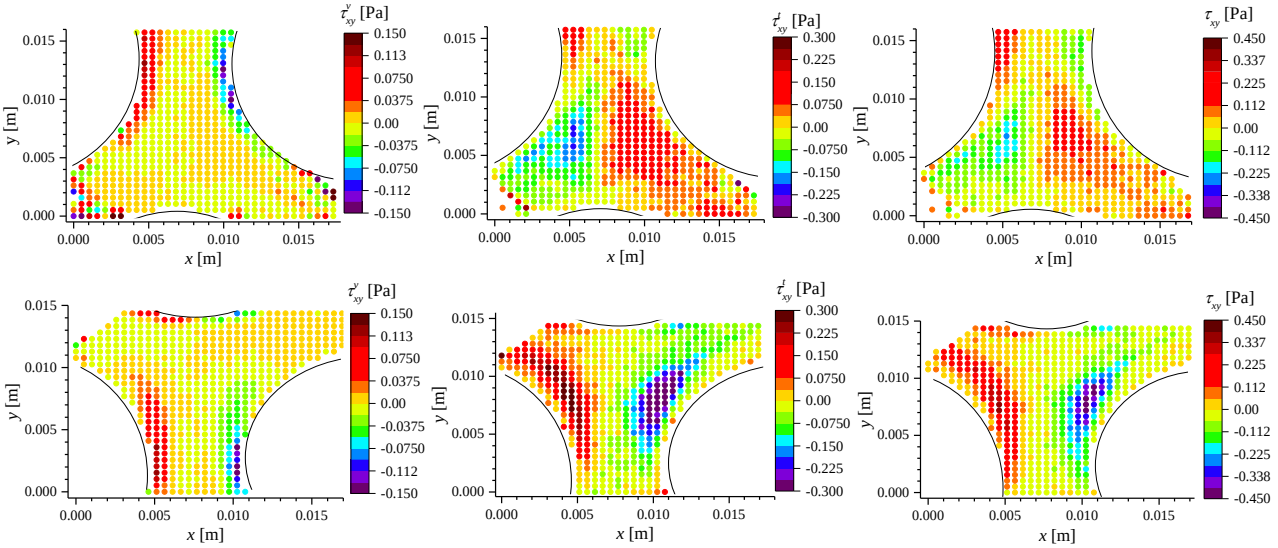

Figure 10: Viscous (τ_{xy}^{v}), Reynolds (τ_{xy}^{t}) and total (τ_{xy}) shear stresses for the Reynolds number of 1842.

The pressure distribution together with the shear stresses around the tubes constitute the total drag and lift forces across the tube bundles. Particularly, the pressure distribution can be obtained from the vector velocity field with the Poisson Equation, considering the small region of analysis as an incompressible flow. The two-dimensional Poisson Equation is obtained by the divergence of the momentum equations (Mathieu and Scott, 2000), resulting in the following equation:

$$\nabla^2 \bar{P} = -\rho \frac{\partial^2}{\partial x_i \partial x_j} \left(\bar{U}_i \bar{U}_j + \overline{u_i u_j} \right) \tag{4}$$

As the vector velocity field obtained by the SFV technique is in discrete form, the pressure distribution obtained by Poisson Equation (Eq. (4)) can be estimated with the partial derivatives approximated by finite differences (Rocha *et*

al., 2017). In this paper, a finite difference scheme of second order was used for all partial derivatives in the entire discrete domain, resulting in a linear matrix equation. In this equation, the pressures are the only unknown variables, which can be solved for traditional methods like Gauss-Seidel method, which is adopted in this study.

A composition of the fundamental regions *Ur* and *Lr* was made to obtain the pressure distribution around an entire tube, as depicted in Fig. 11. Based on the geometry of the tube bundle test section and considering fully developed flow, three data sets of the *Ur* and *Lr* regions were used to compose a region of interest, which comprises all the flow structure and repeats over the test section. In addition to representing a region that encompasses much of the flow structure, the region of interest depicted in Fig. 11 facilitates the application and solution of Eq. 4, because the right and upper boundaries can be used as a boundary condition for the left and bottom boundaries, respectively, and vice versa due to assumption of developed flow. The no-slip condition together with the momentum equations were used to obtain the following equation:

$$\nabla \bar{P} = \rho \left[\nu \frac{\partial^2 \bar{U}_i}{\partial x_j \partial x_j} - \frac{\partial \overline{u_i u_j}}{\partial x_i} \right] \tag{5}$$

which is used as a boundary condition on the wall of the tube. It should be mentioned that the resulting pressure distribution is relative to a given reference point of the flow domain, hence negative values attain for lower values than reference.

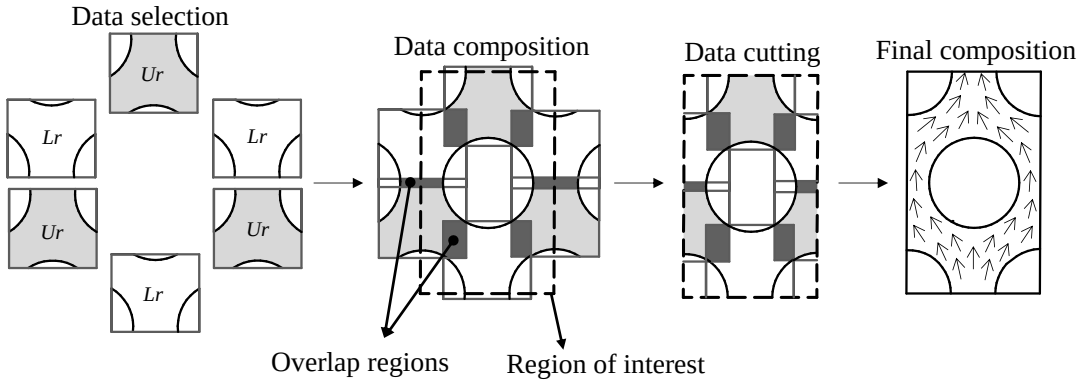

Figure 11: Data composition method for the Poisson equation application.

As can be seen in Fig. 11, the data composition generates overlap regions, where the velocities of the regions *Ur* and *Lr* are superimposed. An overlap procedure, depicted in Fig. 12, was applied to obtain representative velocities in the intersection regions, which consists in estimating a velocity v_c based on weighting values (w) and on the velocity values of each data sample in the same interrogation area (v_{Lr} and v_{Ur}), as follows:

$$v_c = w_{Ur}.v_{Ur} + w_{Lr}.v_{Lr} \tag{6}$$

To avoid discontinuities of the velocity values in the region of interest, the weightings are calculated in the overlap regions with the maximum distances (d) of the calculated velocity point from each data samples, according to the following relationships:

$$w_{Ur} = \frac{d_{Lr}}{d_{Lr} + d_{Ur}} \tag{7}$$

$$w_{Lr} = \frac{d_{Ur}}{d_{Lr} + d_{Ur}} \tag{8}$$

where d_{Lr} and d_{Ur} are the maximum distances of the calculated velocity point from the data samples *Lr* and *Ur* out of the overlap region, respectively. As can be seen in Fig. 12, Eqs. 7 and 8 generate smooth surfaces of weightings, which provide smooth transitions between the data samples. Nonetheless, the consideration of the overlapping velocities has the potential to improve the estimation of pressure profiles around an entire tube.

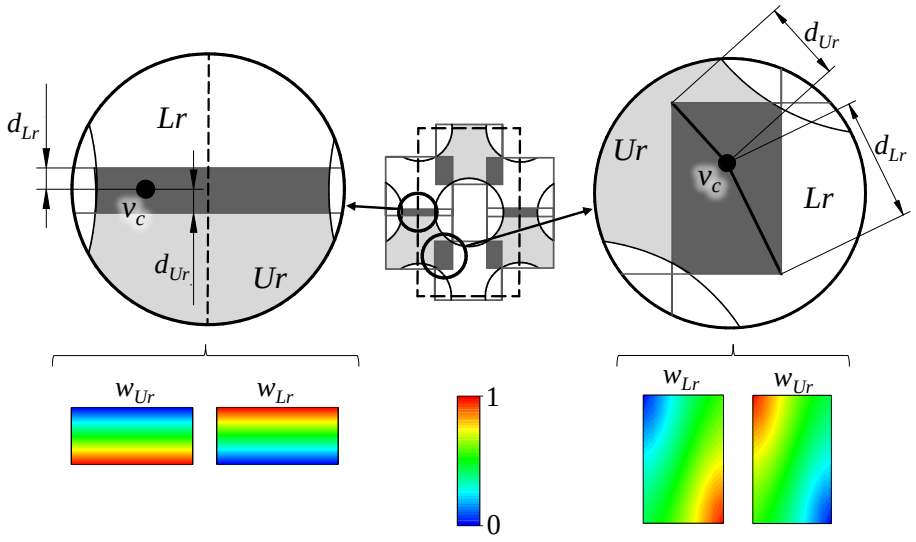

Figure 12: Overlap procedure to obtain representative velocities in the intersection regions.

Fig. 13 shows the pressure distribution for the results depicted in Fig. 4 obtained according to the method aforementioned. The results presented in Fig. 13 agree with expected because the maximum pressure difference increases with the water flow rate, and the regions of minimum and maximum pressures occur in the regions of maximum and minimum velocities, respectively. The results lose symmetry according to the water flow rate increasing. This fact occurs mainly because of the chaos of turbulent flows, which have high-velocity fluctuations and are more susceptible to flow separation.

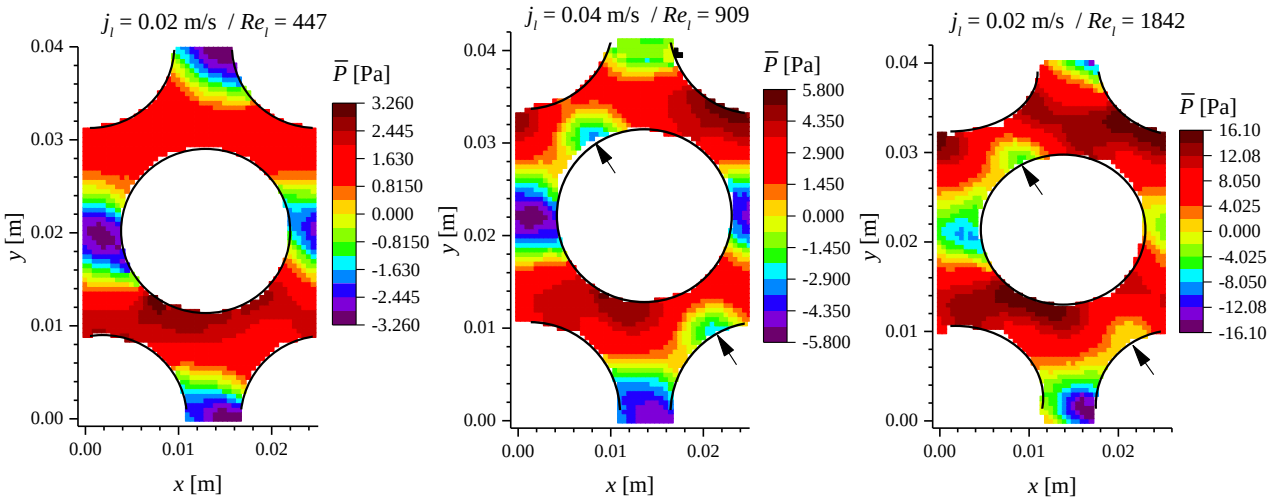

Figure 13: Pressure distribution of the vector velocity fields presented in Fig.4 combined according to the Fig. 11 and 12. The recirculating zone of the experiments with Reynolds number of 909 and 1842 are highlighted by the narrows.

The high pressures of the stagnation points upstream the tubes are observed in all experimental conditions presented in Fig.13. Furthermore, the recirculating zones observed in Fig. 4 can be identified in Fig. 13 in regions of low pressure just downstream the tubes horizontal centerlines for Re_l of 909 and 1842. However, for the experiment with Reynolds number of 447 the local low-pressure zone downstream the tube is not identified, because there is no recirculating zone in this experimental condition, as depicted in Fig.4.

In this context, the high pressures difference between upstream and downstream the tubes can increase the drag force, which is related to pressure drop, and induces flow vibration on the tube in the case of variable pressure field along time.

The results presented in Figs. 10 and 13 show that the SFV technique can provide detailed results, not only of the flow structure but also of the shear stress and pressure distribution along the tube bundles. The results presented in Figs. 4 to 13 allow to better understand the flow phenomenology and are promising to analyze the pressure loss and the flow-induced vibrations.

6. CONCLUSIONS

This paper presents an experimental study of the velocity profile across a triangular tube bundle test section, where the flow vorticity, the turbulence strength, the shear stress distribution and the pressure distribution were analyzed. From the experimental results, the general conclusions of this study are listed as follows:

- The SFV technique provides satisfactory results of the vector velocity field in tube bundles test sections, as validated by comparison with volumetric flow rate. Additionally, this technique is capable of capturing the asymmetric distribution in the velocity field in all experimental conditions, which switch from time to time, indicating the bistable behavior of the flow for reduced Reynolds numbers, as described for De Paula *et al.* (2012).
- The flow separation observed in the vector velocity field directly affected the flow vorticity, the turbulence strength, and the shear stress distribution. The highest and lowest values of these parameters mainly occurred close to separation zone because of the high-velocity gradient. The greatest effects were observed in the experiments with the highest Reynolds number.
- The turbulence strength represents a significant parcel of the total shear stress, especially for the experiments with highest Reynolds number. Additionally, in general, the viscous shear stress is dominant close to solid walls. It should be emphasized that the SFV technique provided valuable results that can be used to infer several flow parameters, such as vorticity and shear stress.
- The results of pressure distribution agree with the flow velocity field. The stagnation region, the recirculating zones and the high and low flow velocities were identified in the pressure distributions showing that the SFV technique provides satisfactory results of the flow structure.

7. ACKNOWLEDGEMENTS

The authors gratefully acknowledge FAPESP (State of São Paulo research foundation agency, Brazil) for the doctorate scholarship (contract number 2016/20200-2) of the first author, Douglas Martins Rocha, and for the internship at Kobe University (contract number 2015/00854-5) of the second author, Fabio Toshio Kanizawa.

8. REFERENCES

De Paula, A.V.; Endres, L.A.M.; Möller, S.V., 2012 “Bistable features of the turbulent flow in tube banks of triangular arrangement”. Nuclear Engineering and Design, v. 249, p. 379-387.

Hosokawa, S.; Mikihara, I.; Tomiyama, A., 2013. “Development of a submersible small fiber LDV probe and its application to flows in a 4 × 4 rod bundle”. Nuclear Engineering and Design, v. 263, p. 342–349.

Hosokawa, S.; Tomiyama, A., 2012. “Spatial filter velocimetry based on time-series particle images”. Experiments in Fluids, v. 52, n. 6, p. 1361–1372.

Iwaki, C.; Cheong, K. H.; Monji, H.; Matsui, G., 2004. “PIV measurement of the vertical cross-flow structure over tube bundles”. Experiments in Fluids, v. 37, n. 3, p. 350–363.

Iwaki, C.; Cheong, K. H.; Monji, H.; Matsui, G., 2005. “Vertical, Bubbly, Cross-Flow Characteristics over Tube Bundles”. Experiments in Fluids, v. 39, n. 6, p. 1024–1039.

Kanizawa, F. T.; Ribatski, G., 2016a. “Two-phase flow patterns across triangular tube bundles for air–water upward flow”. International Journal of Multiphase Flow, v. 80, p. 43–56.

Kanizawa, F. T.; Ribatski, G., 2016b. “Void fraction predictive method based on the minimum kinetic energy”. Journal of the Brazilian Society of Mechanical Sciences and Engineering, v. 38, n. 1, p. 209–225.

Kanizawa, F.T., 2016. *Characterization of external two-phase flow across tube bundles*. Final Report of post doctoral internship at Kobe University, Japan, University of São Paulo, São Carlos School of Engineering, São Carlos, Brazil.

Mathieu, J.; Scott, J., 2000. *An introduction to turbulent flow*. Cambridge University Press.

Paul, S. S.; Tachie, M. F.; Ormiston, S. J., 2007. “Experimental study of turbulent cross-flow in a staggered tube bundle using particle image velocimetry”. International Journal of Heat and Fluid Flow, v. 28, n. 3, p. 441–453.

Rocha, D. M., Kanizawa, F. T., Ribatski, G., 2017. “Experimental analysis of single-phase external flows across tuble bundles using spatial filter velocimetry”. *In Proceedings of the Simpósio do Programa de Pós-Graduação em Engenharia Mecânica - 2o SiPGEM 2017*. University of São Paulo, São Carlos, Brazil.

9. RESPONSIBILITY NOTICE

The authors are the only responsible for the printed material included in this paper.